PERGAMON

International Journal of Solids and Structures 36 (1999) 4397–4423

INTERNATIONAL JOURNAL OF SOLIDS and STRUCTURES

In-plane biaxial crushing of honeycombs—Part II: Analysis

S.D. Papka, S. Kyriakides*

Research Center for Mechanics of Solids, Structures and Materials, The University of Texas at Austin, WRW 110, Austin, TX 78712, U.S.A.

Received 26 February 1998; in revised form 4 July 1998

Abstract

The in-plane biaxial crushing experiments on polycarbonate honeycomb presented in Part I are simulated using large scale finite element models. The models account for nonlinearities in geometry and due to contact while the polycarbonate is modeled as an elastic-powerlaw viscoplastic solid. Full-scale simulations of the uniaxial crushing of this honeycomb were shown in the past to reproduce experiments with accuracy. In biaxial crushing, it was not practical to model specimens the same size as those in the experiments due to computational limitations; instead, a smaller model with 10×11 cells was adopted. Results from simulations of seven of the crushing experiments in Part I with various biaxiality ratios are presented. Through parametric studies it is demonstrated that the size of the specimen and friction between the specimen and the loading surfaces affect the initial elastic parts of the stress–displacement responses and the onset of instability. By contrast, for average crushing strains higher than approximately 10%, their effect was relatively small and the calculated responses were in good agreement with the experimental ones. As a consequence, the energy absorption capacity was predicted to good accuracy for all biaxiality ratios. In addition, many of the modes of cell collapse seen in the experiment are reproduced in the simulations.

1. Introduction

The biaxial crushing behavior of the circular cell polycarbonate honeycomb studied experimentally in Part I of this two part series of papers, is complex and projects as a very challenging modeling task. In addition to the geometric nonlinearities involved, the material is inelastic and rate dependent, frictional contact between the edge cells and the platens must be accounted for, and the complex contact between the walls of the collapsing cells must be properly modeled. In the simpler case of uniaxial crushing in the y-direction, Papka and Kyriakides (1998a)[1] demonstrated that, provided the geometric and contact nonlinearities are carefully modeled and the

* Corresponding author. Fax: 001 512 471 5500; e-mail: skk@mail.utexas.edu

[1] Refer to figures, references and Tables in Part I.

0020-7683/99/$ - see front matter
PII: S0020-7683(98)00225-X

material nonlinearities of the polycarbonate are properly attended to it is possible for the crushing response to be calculated to very good accuracy. Full scale finite element (FE) simulations of the crushing responses were shown to reproduce all features of the experimental results. In this paper we extend these schemes to the biaxial setting and evaluate their performance by comparing predictions with the experimental results in Part I.

Efforts made to date to model the large deformation of honeycombs under biaxial loads have been few and addressed mainly hexagonal honeycomb. Klingworth and Stronge (1988)[1] used idealized plastic hinge models to establish yield limits under biaxial compression and compression and shear. Similar schemes where also used in Zhang and Ashby (1992)[1] for similar considerations. More recently, Triantafyllidis and Schraard (1998)[1] conducted a more rigorous study of the same general problem using carefully selected representative microsections which were then analyzed numerically to produce initial failure surfaces for biaxial crushing of aluminum honeycombs with the same characteristics as those in the study of Papka and Kyriakides (1994)[1]. Gibson et al. (1989) and Triantafyllou et al. (1989) examined the onset of yielding in foams under multiaxial loads with the support of experiments (Triantafyllou and Gibson, 1990). The objective of the present effort is to simulate the circular cell honeycomb response all the way to densification in order to establish its energy absorption capacity.

2. Constitutive modeling of the polycarbonate

The mechanical behavior of the polycarbonate material of the honeycomb was established through a set of uniaxial tension tests on tubes from the same batch as those used to manufacture the honeycomb. The test specimens were typically 11 tube diameters long. Six constant strain rate tests were conducted at rates ranging from 10^{0}–10^{-5} s^{-1}. This range nearly spans the strain rates of the deformations experienced by the honeycomb material in the lateral crushing experiments presented in Part I. Each test was terminated shortly after the appearance of a neck in the test section of the specimen.

The six stress–strain responses measured are shown in Fig. 1. The initial linear parts of the responses coincide indicating that in this strain rate regime elastic deformations can be considered to be rate independent. By contrast, the subsequent inelastic parts of the responses are seen to exhibit significant rate sensitivity.

This nonlinear material behavior was modeled as a powerlaw viscoplastic solid. Strain rates are assumed to consist of an elastic part and an inelastic part

$$\dot{\varepsilon}_{ij} = \dot{\varepsilon}^{e}_{ij} + \dot{\varepsilon}^{p}_{ij}. \tag{1}$$

Elastic deformations are linear and isotropic and are related to stresses by

$$\dot{\varepsilon}^{e}_{ij} = \frac{1+v}{E}\dot{\sigma}_{ij} - \frac{v}{E}\dot{\sigma}_{kk}\delta_{ij} \quad \text{or } \dot{\sigma}_{ij} = C_{ijkl}(E, v)\dot{\varepsilon}^{e}_{kl} \tag{2}$$

where E is the Young's modulus and v the Poisson's ratio of the material both assumed to be independent of rate (values given in Table 1).

The rate dependence of the inelastic part of the deformation ($\dot{\varepsilon}^{p}_{ij}$) is assumed to obey a power law which for a uniaxial state of stress and strain is given by

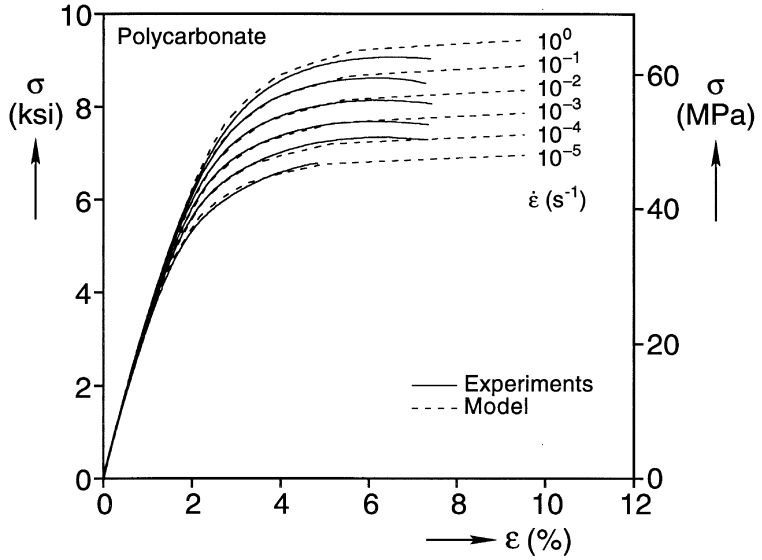

Fig. 1. Stress–strain responses of polycarbonate at various strain rates and corresponding predictions.

Table 1
Material parameters used in elastic–viscoplastic constitutive model

E ksi (GPa)	ν	σ_0 ksi (MPa)	m	ξ
350 *(2.41)	0.3	3.0 (20.7)	0.027	0.25

$$\left(\frac{\dot{\varepsilon}^{\mathrm{p}}}{\dot{\varepsilon}_0}\right)^m = \frac{\sigma}{\Sigma(\varepsilon^{\mathrm{p}})}. \tag{3}$$

Here, $\dot{\varepsilon}_0$ is a reference strain rate, $\Sigma(\varepsilon^{\mathrm{p}})$ is the flow stress measured when $\dot{\varepsilon}^{\mathrm{p}} = \dot{\varepsilon}_0$, and m is the rate exponent. In this case, $10^{-3}\ \mathrm{s}^{-1}$ was chosen as the reference rate. The yield stress (σ_0) was selected to be 3 ksi (20.7 MPa) and the inelastic part of the response was fitted with a multilinear fit (11 segments of variable strain spans). The value of the rate exponent was found in the usual way to be 0.027. The fit is drawn with a dashed line in Fig. 1 along with the predicted responses for the other five strain rates. The results of the model are seen to be in good agreement with the measured responses for all cases up to a strain of approximately 5% when the deformation in the tubes started to become inhomogeneous due to necking (not an issue in the honeycomb where bending deformations are dominant).

The model was generalized to the multiaxial setting through the classical associative plasticity framework. The plastic strain rate is give by

$$\dot{\varepsilon}_{ij}^{\mathrm{p}} = \Lambda \frac{\partial f}{\partial \sigma_{ij}} \tag{4}$$

with the following choice for f:

$$f = \sigma_{\mathrm{e}} = \sqrt{\tfrac{3}{2} s_{ij} s_{ij}}, \quad s_{ij} = \sigma_{ij} - \tfrac{1}{3}\sigma_{kk}\delta_{ij}. \tag{5}$$

A work compatible measure of equivalent plastic strain rate is given by

$$\dot{\varepsilon}_{\mathrm{e}}^{\mathrm{p}} = \sqrt{\tfrac{2}{3} \dot{\varepsilon}_{ij}^{\mathrm{p}} \dot{\varepsilon}_{ij}^{\mathrm{p}}}. \tag{6}$$

Thus (3), (5) and (6) $\rightarrow$(4) yield

$$\dot{\varepsilon}_{ij}^{\mathrm{p}} = \dot{\varepsilon}_{\mathrm{e}}^{\mathrm{p}} \left(\frac{3}{2} \frac{s_{ij}}{\sigma_{\mathrm{e}}} \right) = \dot{\varepsilon}_0 \left(\frac{\sigma_{\mathrm{e}}}{\Sigma(\varepsilon_{\mathrm{e}}^{\mathrm{p}})} \right)^{1/m} \left(\frac{3}{2} \frac{s_{ij}}{\sigma_{\mathrm{e}}} \right) \tag{7}$$

where

$$\varepsilon_{\mathrm{e}}^{\mathrm{p}} = \int_0^t \dot{\varepsilon}_{\mathrm{e}}^{\mathrm{p}} \, \mathrm{d}t. \tag{8}$$

By combining (2) and (3) through (1) and inverting we arrive at

$$\dot{\sigma}_{ij} = C_{ijkl}\dot{\varepsilon}_{kl} - \left(\frac{3\dot{\varepsilon}_{\mathrm{e}}^{\mathrm{p}}}{2\sigma_{\mathrm{e}}} \right) C_{ijkl} s_{kl}. \tag{9}$$

For numerical expediency, the value of $\dot{\varepsilon}_{\mathrm{e}}^{\mathrm{p}}$ in a given time increment was evaluated through the forward gradient method of Peirce et al. (1984) with the rationing parameter $\xi = 0.25$ (see Papka, 1998[1]). Problems involving localization and propagation of deformation place extra demands on rate dependent constitutive models due to significant changes in the local rate of deformation. For this reason, extra effort was placed in ensuring that the model could meet these challenges. More on this can be found in Papka and Kyriakides (1998a)[1] and Papka (1998)[1].

We emphasize that this model is chosen primarily due to its relative simplicity but also due to its proven performance in reproducing the nonlinear material features required in this type of application. Its adoption should not be interpreted as an endorsement for a more universal use for modeling complex viscoelastic/viscoplastic behavior of polymers in which, for example, inelastic incompressibility is known to not apply.

3. Finite element models

3.1. Geometry

The geometric characteristics of the honeycomb were established by careful measurements under a microscope connected to an image processing system. Listed in Table 2 are mean values and

Table 2
Geometric characteristics of honeycomb cells

	D in (mm)	t in (μm)	ϕ°	Δ_0 (%)
Mean value	0.274 (6.96)	0.00568 (144)	10.5	4.88
SD	0.002 (0.051)	0.00025 (6.4)	1.9	1.82

standard deviations (SD) of the cell diameter (D) and wall thickness (t) (see Fig. 7a in P&K, 1998[1]). The cells were not perfectly circular (see Fig. 8a in Papka and Kyriakides, 1998[1]) and the deviation is reported in the form of ovality (Δ_0) defined as follows

$$\Delta_0 = \frac{D_{\max} - D_{\min}}{D_{\max} + D_{\min}}. \tag{10}$$

The cells are bonded to each other along arcs spanning an angle ϕ° (see Fig. 8b in Papka and Kyriakides, 1988a)[1] values of which are also included in Table 2.

In the numerical simulations that follow the cells are circular and are in a hexagonal arrangement as was done in Papka and Kyriakides (1998a)[1] for uniaxial crushing. We use the mean values of diameter, wall thickness and bond line listed in Table 2. The cell ovality was randomly distributed and is neglected. Neglecting the imperfections affects to a small degree the onset of the instability but has only a minor effect on the response in the large deformation regime.

In the simulations of the two uniaxial crushing tests, the honeycomb geometry is essentially the same as in the tests. In the biaxial tests, adhering to the 18×21 cell size of the specimens tested would have made the size of the problem too large for the computational facilities available to us. We thus opted for a 10×11 cell specimen (2.740×2.647 in—69.6×67.2 mm) for all simulations. The implications of this will be discussed in the presentation of the results.

3.2. Discretization

The problem was discretized using quadratic beam elements (ABAQUS) based on nonlinear kinematics which allow for finite rotations and finite membrane strains. Because the out-of-plane thickness of the honeycomb was approximately five times the cell diameter, the elements were modified so that the deformation of the tubular cells was cylindrical. The bonded arcs of the cells were modeled by connecting nodes on either side of the bond with rigid beam elements. Each cell was modeled by 24 unevenly distributed elements. The distribution of elements around the circumference of the cells was chosen such that the extent of the bond line could be modeled accurately. Each element had two integration points along the length and nine through the thickness.

A major difficulty in the problem is the contact between the walls of collapsing cells. In uniaxial crushing, contact was modeled by predefining a pair of contact surfaces. ABAQUS then generates

the contact elements automatically. This option also allows for finite sliding between the contacting surfaces. In biaxial crushing, in general, the collapse of the cells is unsymmetric and irregular. As a result, the contact is added when and where it is needed as the simulation progresses. Since the contact must be defined at the start of the analysis, this often resulted in a trial and error process to determine the proper location to define the contact surfaces. Each contact surface pair was defined by identifying the location and direction of contact. In this case contact was frictionless with finite sliding allowed.

In the case of biaxial crushing, contact between adjacent cells can also take place in the triangular hypocycloidal regions. This contact was also modeled by predefining each pair of contact surfaces. However, since the surfaces between adjacent cells are restricted from sliding relative to one another, a frictionless, small sliding option was used for computational efficiency.

4. Simulation of uniaxial crushing

4.1. y-*crushing*

Uniaxial crushing in the y-direction was discussed extensively in Papka and Kyriakides (1998a)[1]. Thus, here we present an overview of the simulation of the experiments in Part I to set the stage for the uniaxial simulations that follow. As in the experiment, the model is crushed between two plates one of which was fixed while the second was prescribed a constant velocity ($\dot{\delta}_y$). Both the contact between the rigid plates and honeycomb and the contact between the walls of collapsed cells were frictionless. The model had more than 27,500 variables (number of degrees-of-freedom + number of Lagrange multipliers). In addition, accurate modeling of viscoplastic behavior and contact between the walls of collapsing cells required that the prescribed velocity increments ($\Delta\dot{\delta}_y$) be small.

The position at which instability initiated was chosen by adding small couples on the walls of the central cells in a selected row of cells. This influences the resulting pattern of crushing but essentially has no other effect on the honeycomb properties of interest. In the results that follow, the instability was initiated in approximately the same row in which it initiated in the corresponding experiment.

We first consider the results of the simulation of the experiment in Fig. 5[1]. The calculated crushing response is plotted together with the corresponding experimental one in Fig. 2a. A sequence of deformed configurations corresponding to the equilibrium points identified on the calculated response is shown in Fig. 2b. Overall, the simulated response is seen to be in very good agreement with the experimental one. In addition, the sequence of events seen in Fig. 2b are very similar to those of the experiment.

The initial modulus, calculated over the same gage length as in the experiment, is 248 psi (1.71 MPa). That is, approximately 5% higher than the measured value. In specimens of relatively small size, like the ones used here, there exists a small gradient in deformation from the edge to the center. Thus, in both the experiments and the simulations, the initial slope of the overall response is lower than the value of E_y^* measured in the 51 mm gage length at the center of the specimen (by approximately 20% in the analysis and 25% in the experiments). For more on the effect of specimen size on the calculated value of E_y^* see Section 4.4 in Papka and Kyriakides (1998a)[1].

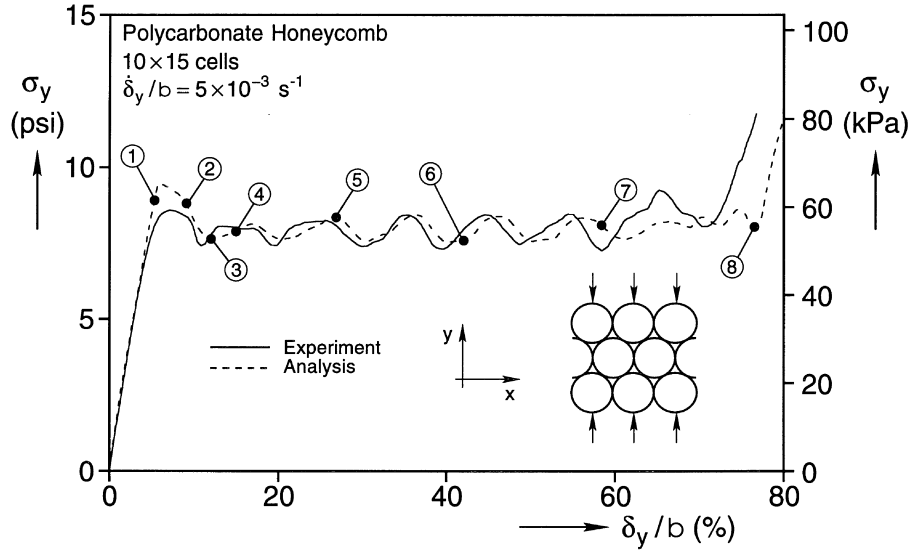

Fig. 2a. Comparison of measured and calculated uniaxial crushing responses in the y-direction of a honeycomb specimen loaded at an average strain rate of 5×10^{-3} s^{-1}.

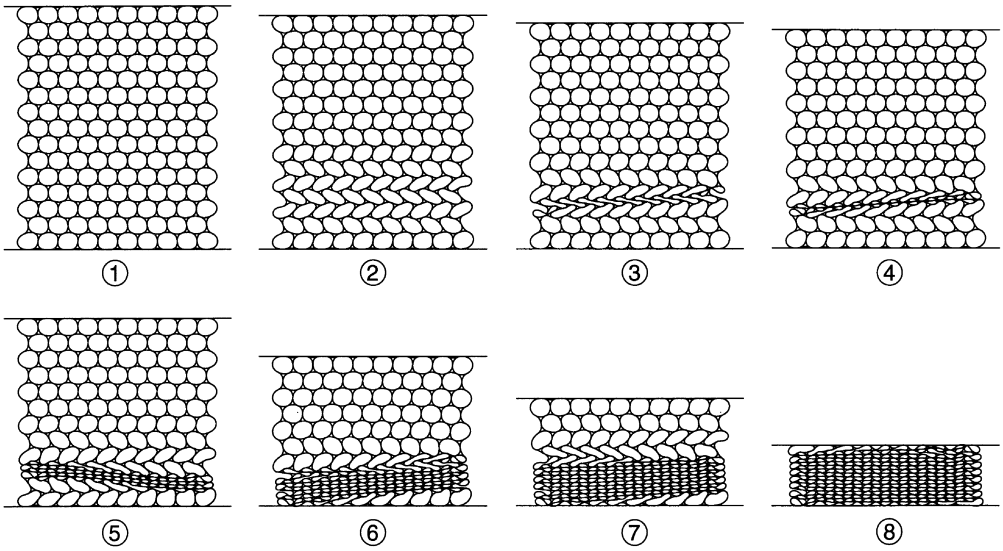

Fig. 2b. Sequence of calculated collapse configurations corresponding to response in Fig. 2a.

The initiation stress is 9.48 psi (65.3 kPa) or 10% higher than the measured value. This difference can be attributed directly to the absence of geometric imperfections such as cell ovalization and wall thickness variations in the model.

After the load maximum, the deformation localizes in the 12th row of cells as shown by

Table 3
Comparison of measured and predicted problem variables in uniaxial crushing
a. y-crushing: $\dot{\bar{\delta}}_y = 5 \times 10^{-3}\ \mathrm{s}^{-1}$

	E_y^* psi (MPa)	σ_{Iy} psi (kPa)	σ_{Py} psi (kPa)	$\Delta\varepsilon_{Py}$ %	$\mathscr{E}_y$ psi (kPa)
Experiment	240 (1.66)	8.60 (59.3)	8.02 (55.3)	63.1	5.33 (36.8)
Analysis	248 (1.71)	9.48 (65.4)	7.99 (55.1)	70.7	5.44 (37.5)

b. x-crushing: $\dot{\bar{\delta}}_x = 5 \times 10^{-3}\ \mathrm{s}^{-1}$

	E_x^* psi (MPa)	σ_{Ix} psi (kPa)	σ_{Px} psi (kPa)	$\Delta\varepsilon_{Px}$ %	$\mathscr{E}_x$ psi (kPa)
Experiment	236† (1.63)	10.5 (72.4)	10.2 (70.3)	63.6	6.69 (46.1)
Analysis	257‡ (1.77)	10.28 (70.9)	10.13 (69.9)	69.0	6.55 (45.2)

† Specimen size: 49×59 cells.
‡ Specimen size: 30×35 cells.

configuration ② and ③. Cells in this region collapse in the unsymmetric shear-type mode mentioned earlier. Soon after configuration ③, the walls of the collapsed row of cells come into contact (see ④) and local deformation is arrested. However, the cells in rows 11 and 13 have been weakened by the collapse of row 12 and, as a result, they collapse next. This process of successive destabilization of a row of cells followed by local collapse continues until the whole specimen has collapsed. In the process a load plateau with undulations is traced. By configuration ⑧ all cells have collapsed and the response then takes a sharp upturn.

Overall, all features of the measured response are well reproduced by the analysis. The average value of the calculated propagation stress is 7.99 psi (55.1 kPa) which compares very well to the experimental value of 8.02 psi (55.3 kPa). In addition, the number of undulations in the stress plateau and their location are well reproduced by the analysis. As mentioned in Part I, each stress peak and valley corresponds to the collapse of two rows of cells. As a result, specimens with more rows of cells have a proportionate number of additional stress peaks. On the other hand, if the specimen width changes, the evolution of events described and the characteristics of the undulations do not change.

Like the initiation load, the extent of the load plateau ($\Delta\varepsilon_{Py}$) is somewhat overpredicted due to the absence of geometric variations in the model. In the actual honeycomb, imperfections can stiffen regions of cells during crushing causing the load to begin to increase earlier than predicted. However, the energy absorbed per unit undeformed volume ($\mathscr{E}_y$, for $\bar{\delta}_y \in [0, 0.70]$) is in very good agreement with the experimental value (Table 3a).

The rate of crushing has an influence on the initiation and propagation stresses measured in

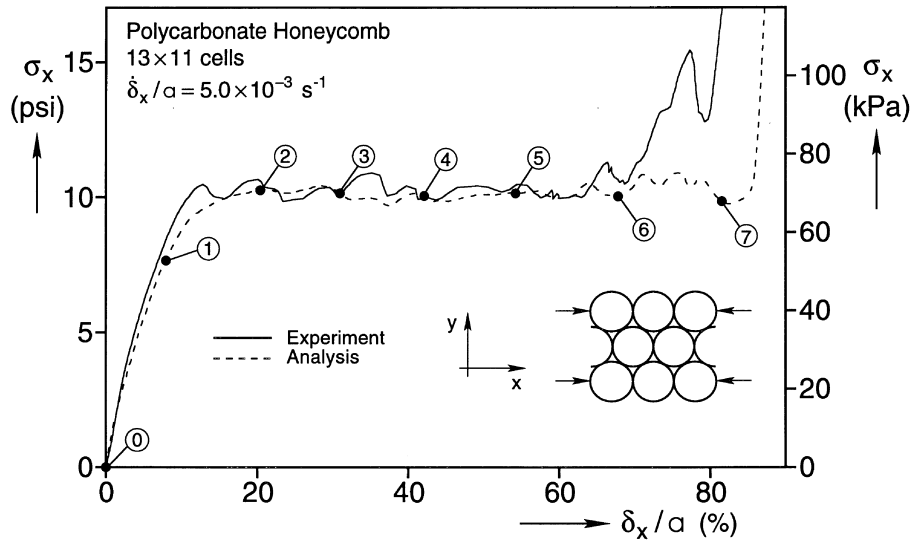

Fig. 3a. Comparison of measured and calculated uniaxial crushing responses in the x-direction of a honeycomb specimen loaded at an average strain rate of 5×10^{-3} s^{-1}

such simulations. This effect was extensively analyzed in P&K (1998a)[1] where the models were shown to capture this effect with good accuracy also.

4.2. x-*crushing*

The simulation of the x-crushing experiment (Fig. 7[1]) is shown in Fig. 3. The calculated σ_x–$\bar{\delta}_x$ response is shown in Fig. 3a along with the corresponding experimental one. A sequence of deformed configurations corresponding to it are shown in Fig. 3b. Overall, the calculated response is in good agreement with the experimental one. The nonlinearity of the initial rising part of the response seen in the experiment is repeated in the calculated response where it is more severe. Once again, this nonlinearity can be attributed to the early crushing of the two edge columns of cells clearly illustrated in ①. In this case, the edges also provide the disturbance necessary to initiate the instability (see ②). The initial localization of collapse is along rows of cells inclined at $\pm60^\circ$ to the x-axis due to the alignment of cells in these directions. A pair of sideways v-shaped collapse patterns develop simultaneously one at each end of the specimen (③). Through this the deformation maintains symmetry about the middle of the specimen. This is similar to what was observed in the experiment where, however, the two patterns developed sequentially. At higher values of $\bar{\delta}_x$, additional zones collapse with similar orientations (④ and ⑤). The symmetry of the collapse pattern is broken near configuration ⑤ and subsequently, the collapsed zones broaden and coalesce as observed in ⑥ and ⑦. Unlike the experiment, in the simulation, collapse is relatively well behaved to the end and, as a result, the last stress spike seen in the experimental response is missing.

The key variables of the simulation are listed in Table 3b along with those from the experiment. The calculated initiation stress is 10.28 psi (70.9 kPa) and the propagation stress is 10.13 psi (69.9

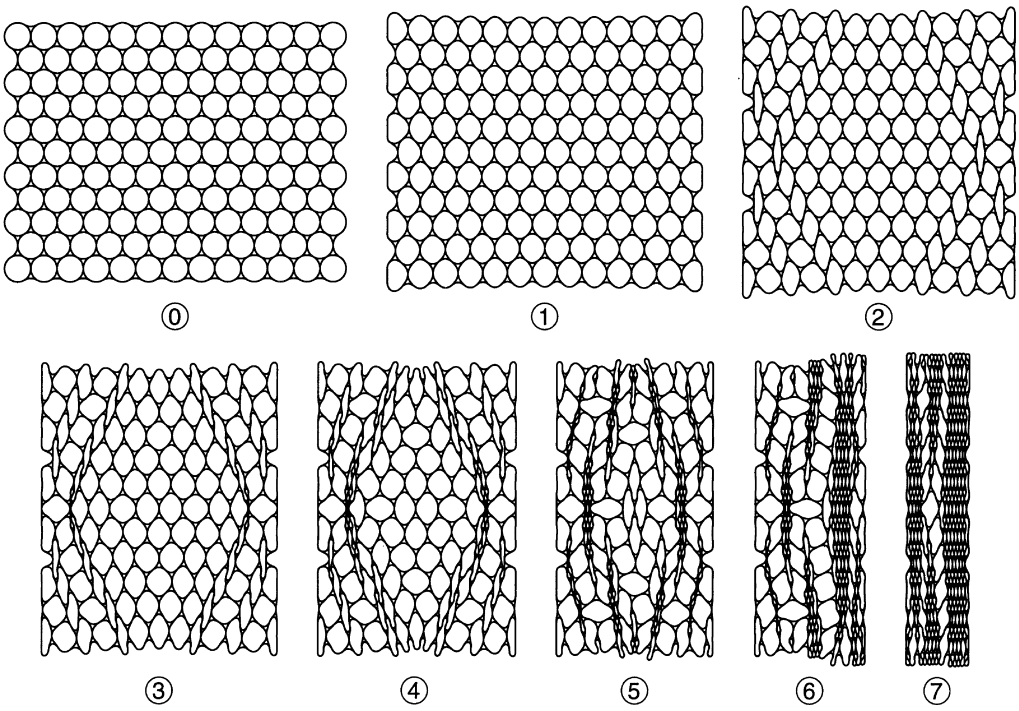

Fig. 3b. Sequence of calculated collapse configurations corresponding to response in Fig. 3a.

kPa), both in very good agreement with the measured values. Thus, the analysis confirms that the initiation stress is only slightly higher than the propagation stress. Because of this, the specific sequence of events seen in any one particular simulation can be altered by factors which, for example, in the y-crushing were not significant. Friction is one of these factors. In the x-crushing simulation, as will be the case in the simulations of the biaxial crushing experiments, friction between the rigid surfaces and the specimen influences the sequence of events that take place primarily due to differences in the way the edge cells collapse. A Coulomb fiction coefficient of 0.1 was used in the simulation shown.

The extent of the stress plateau is approximately the same as that in the y-crushing test. Since the propagation stress is approximately 27% higher, the energy absorption capacity ($\mathscr{E}_x$, for $\bar{\delta}_x \in [0, 0.70]$) is more than 20% higher than $\mathscr{E}_y$.

Finally, a word about the elastic modulus E_x^*. As mentioned in Part I, this proved to be a very difficult variable to measure accurately first due to its sensitivity to specimen size and second due to the sensitivity of the measurement to small edge misalignments of the specimen. The measurement quoted in Table 3b came from a 49×59 cells specimen whose edges were specially trimmed to ensure that they were close to being parallel. The predicted value came from the largest size specimen our computer would accept which was 30×35 cells. The difference between the measured and calculated values in Table 3b is partly due to the difference in specimen size but, perhaps more importantly, also due to errors introduced in the experiment from geometric imperfections and specimen misalignments.

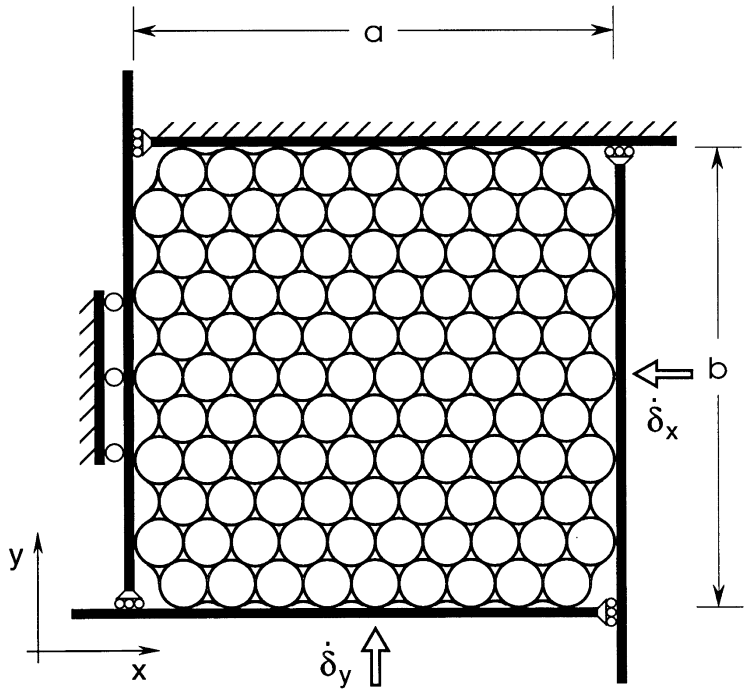

Fig. 4. Geometry of honeycomb specimens used in biaxial crushing analyses.

5. Simulation of biaxial crushing

In order to keep the size of the problem at a level manageable by the computer facilities available to us, the size of the specimen in all biaxial simulations was chosen to have 10×11 cells (see Fig. 4). This contrasts with the experimental specimen size of 18×21 cells. Even at this smaller size, the number of variables in the model were in excess of 30,000. We varied the specimen size in both the experiments and in the simulations sufficiently to know that it affects, first and foremost, the elastic properties, second the onset of instability, and thirdly to a lesser degree the collapse patterns. By contrast, the inelastic parts of the responses, including the energy absorption capacity, are affected significantly less by specimen size at least when the size reduction is of the order of the one we adopted. In what follows, we will present results from numerical simulations of seven of the biaxial experiments and will compare the results with the experimental ones despite this difference in specimen size. Wherever possible we will try to illustrate how the specimen size affects the results.

The discretized honeycomb is surrounded by four rigid surfaces as shown in Fig. 4. The top surface is fixed but the other three move in the same way as the platens of the BICRUMA in order to match the frictional characteristics of the physical test. Thus, the right and bottom surfaces are prescribed constant displacement rates $(\dot{\delta}_x, \dot{\delta}_y)$, respectively, while the bottom surface also slides to the left and the left surface slides upwards. The velocities are chosen so that the average 'strain' rates $(\dot{\delta}_x/a, \dot{\delta}_y/b)$ have the same values as those of the corresponding experiments. Matching the

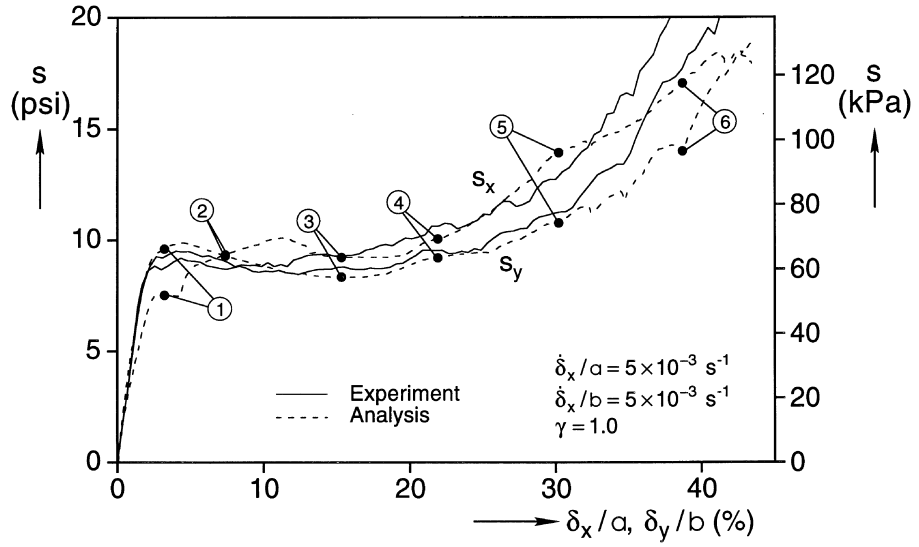

Fig. 5a. Comparison of measured and calculated true stress–displacement responses for equibiaxial crushing.

average 'strain' rate is appropriate for the homogeneous parts of the deformation but is somewhat of a compromise for localized deformation. If we assume that localized zones of collapse have the same size in the smaller specimen as in the larger test specimen, then under this scheme the local rate of deformation will be somewhat smaller in the simulation. However, this difference is not large enough to impact the results in a significant way. Coulomb friction with a coefficient (μ) of 0.1 was assumed between the four surfaces and the honeycomb.

5.1. *Equibiaxial test*: $\gamma = 1.0$, $\dot{\bar{\delta}}_x = 5.1 \times 10^{-3}\, s^{-1}$

Results from the simulation of the equibiaxial test are shown in Fig. 5. Figure 5a shows the calculated true stress–displacement responses along with those from the experiment and Fig. 5b shows a set of six deformed configurations. Overall, the responses can be said to be in reasonably good agreement with the experimental ones. As expected, the predictions differ the most from the measured results in the initial relatively stiff part and around the first knee of the two responses. These differences are more pronounced in the s_x–$\bar{\delta}_x$ responses than those of the y-direction. For values of average strains of approximately 5–35%, the predicted and measured responses are quite similar. Beyond 35%, the material has densified and the measured stiffnesses are somewhat higher than those of the simulation,

The main problem variables yielded by the simulation are listed in Table 4 (see Table 2[I] for corresponding experimental values). The initiation stresses in the x- and y-directions are 10 and 12% higher than the experimental values while the energy absorbed per unit undeformed volume ($\hat{\mathscr{E}}$) evaluated at a volume change of 65% is approximately 6% higher.

The deformation patterns seen in Fig. 5b have similarities to those seen in the experiment. Because of the smaller size of the model, edge effects play a bigger role in the events, but the central part of the specimen does develop the flower-like pattern seen in the experiments. In configurations

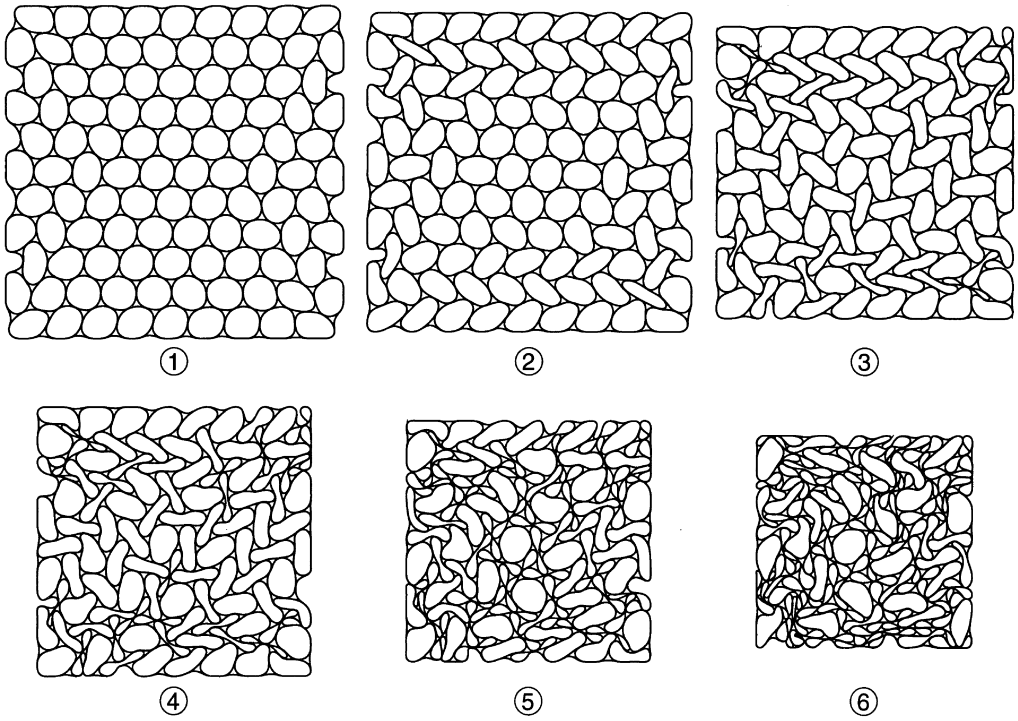

Fig. 5b. Sequence of calculated collapse configurations corresponding to responses in Fig. 5a.

Table 4a
Prediction of problem variables in biaxial crushing of various values of γ and $\dot{\bar{\delta}}_x = 5 \times 10^{-3}\ s^{-1}$

$\dot{\bar{\delta}}_x\ s^{-1}$	$\dot{\bar{\delta}}_y\ s^{-1}$	γ	$\hat{\sigma}_{Ix}$ psi (kPa)	$\hat{\sigma}_{Iy}$ psi (kPa)	$\hat{\mathscr{E}}_x$ psi (kPa)	$\hat{\mathscr{E}}_y$ psi (kPa)	$\hat{\mathscr{E}}$ psi (kPa)
5×10^{-3}	0	0	10.9 (75.2)	7.10 (50.0)	6.45 (44.5)	0	6.45 (44.5)
5×10^{-3}	2.5×10^{-3}	0.5	10.4 (71.7)	9.52 (65.7)	4.62 (31.9)	1.91 (13.2)	6.53 (45.0)
5×10^{-3}	5×10^{-3}	1	10.1 (69.7)	9.88 (68.1)	3.47 (23.9)	3.15 (21.7)	6.62 (45.7)
5×10^{-3}	15×10^{-3}	3	6.98 (48.1)	10.7 (73.8)	1.22 (8.4)	4.66 (32.1)	5.88 (40.6)

④ and ⑤, we can see several cells remain relatively undeformed while the six cells surrounding them deform in the same rotary manner shown in Fig. 11[1].

To better illustrate the nature of this pattern, we extracted from the solution a cluster of cells which exhibit this behavior and plotted it enlarged at several stages of deformation in Fig. 6. Although the hexagonal symmetry alluded to in the corresponding experiment is not perfectly

Table 4b
Prediction of problem variables in biaxial crushing of various values of $1/\gamma$ and $\dot{\bar{\delta}}_y = 5\times10^{-3}\ \mathrm{s}^{-1}$

$\dot{\bar{\delta}}_x\ \mathrm{s}^{-1}$	$\dot{\bar{\delta}}_y\ \mathrm{s}^{-1}$	$1/\gamma$	$\hat{\sigma}_{Ix}$ psi (kPa)	$\hat{\sigma}_{Iy}$ psi (kPa)	$\hat{\mathscr{E}}_x$ psi (kPa)	$\hat{\mathscr{E}}_y$ psi (kPa)	$\hat{\mathscr{E}}$ psi (kPa)
0	5×10^{-3}	0	5.34 (36.8)	10.5 (72.4)	0	5.21 (35.9)	5.21 (35.9)
2.5×10^{-3}	5×10^{-3}	0.5	6.98 (48.1)	10.5 (72.4)	1.98 (13.7)	4.36 (30.1)	6.34 (43.7)
5×10^{-3}	5×10^{-3}	1	10.1 (69.7)	9.88 (68.1)	3.47 (23.9)	3.15 (21.7)	6.62 (45.7)
15×10^{-3}	5×10^{-3}	3	10.3 (71.0)	8.92 (61.5)	5.36 (37.0)	1.22 (8.4)	6.58 (45.4)

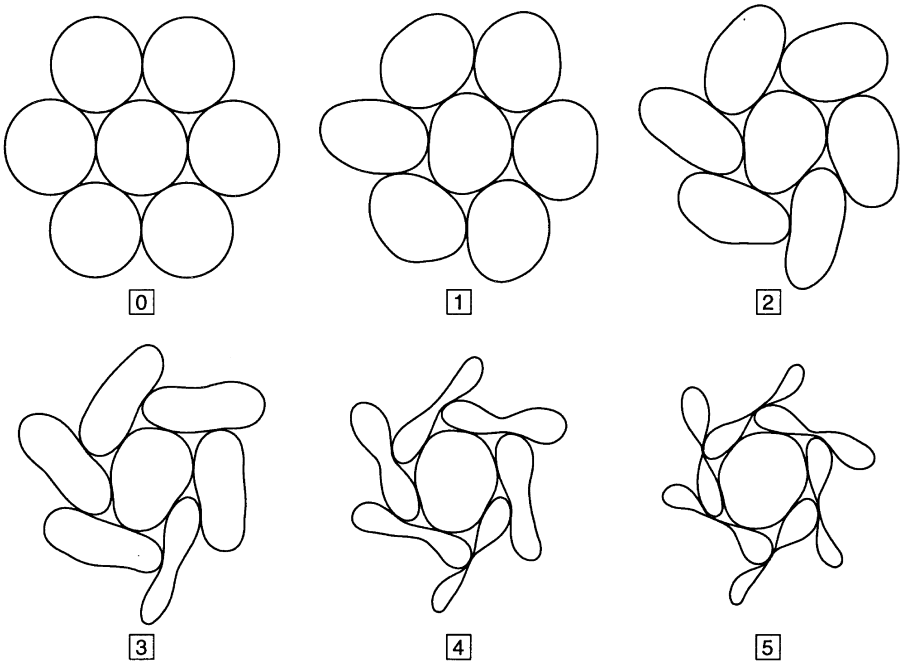

Fig. 6. Cluster of cells extracted from equibiaxial crushing simulation demonstrating a collapse mechanism.

maintained here, due to interference from the edge cells, the pattern does clearly resemble that seen in the experiment.

Before the onset of instability in the interior of the specimen, the x-response exhibits a small local stress plateau at a stress level of approximately 7.5 psi (51.7 kPa) which extends for just under 2% of net strain. Subsequently, the stress rises and traces a path resembling the experimental one. This is a feature absent from the experimental results and was investigated in some detail.

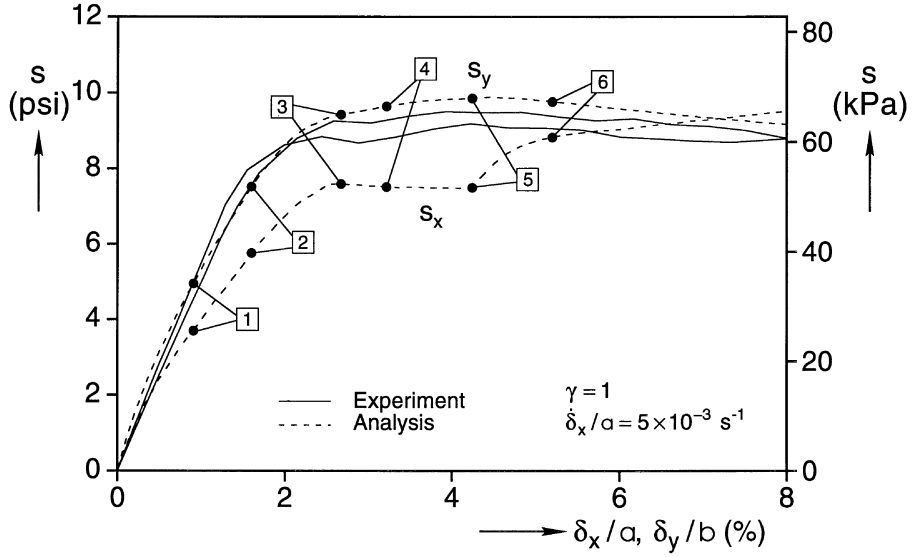

Fig. 7a. Comparison of measured and calculated stress–displacement responses during the early part of the crushing process.

Figure 7a shows an expanded view of the early parts of the calculated and measured responses and Fig. 7b shows six deformed configurations corresponding to equilibria before, during, and after this feature. The expansion of the strain scale brings out more vividly the fact that the calculated response is less stiff right from the start. The main cause of this difference is that in the perfectly aligned specimen of the simulation, the edge cells in contact with the two vertical surfaces deform significantly more. They can be seen to flatten as early as in configurations [1] at a stress of just over 3 psi (20 kPa). The flattening grows in [2] and, as the material becomes plasticized, they lose further stiffness and start to collapse. The small plateau is associated with their collapse (see [3]–[5]). As we will see below, the extent of this collapse and, as a result, that of the stress plateau is limited by friction. While this stress plateau is traced, the interior of the specimen remains relatively undeformed. By contrast, in the experiment, even in configuration ① in Fig. 10b[1] which corresponds to a stress level well before the knee in the response, we see that deformation has spread to the interior of the specimen. At the same time, the edge cells are not deformed as much or as uniformly as in the simulation. Small geometric irregularities present in the honeycomb tested are responsible for this difference in behavior.

This localized flattening and collapse of the edge cells is also responsible for the lower initial stiffness in the calculated s_x–$\bar{\delta}_x$ response. The test specimen in the simulation is only 10 cells wide as opposed to 18 in the test. Thus, localized deformation in the two columns of cells at the edges, averaged over a smaller initial specimen width (a) results in a smaller apparent stiffness. To illustrate this point further, we conducted similar calculations using a 14×17 cells specimen (limited to the early part of the response before walls of collapsing cells come into contact). The deformation of the cells of the larger specimen were very similar to those of the smaller one in Fig. 7b. The two pairs of stress–normalized displacement responses are compared in Fig. 8. For the larger specimen,

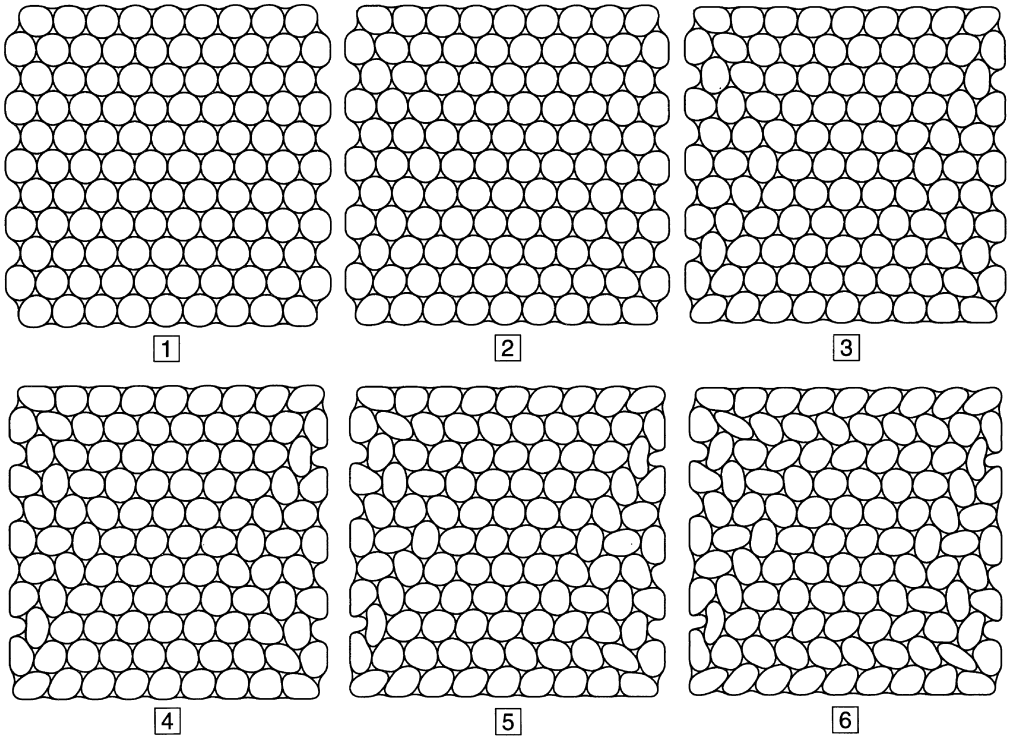

Fig. 7b. Sequence of calculated collapse configurations corresponding to responses in Fig. 7a.

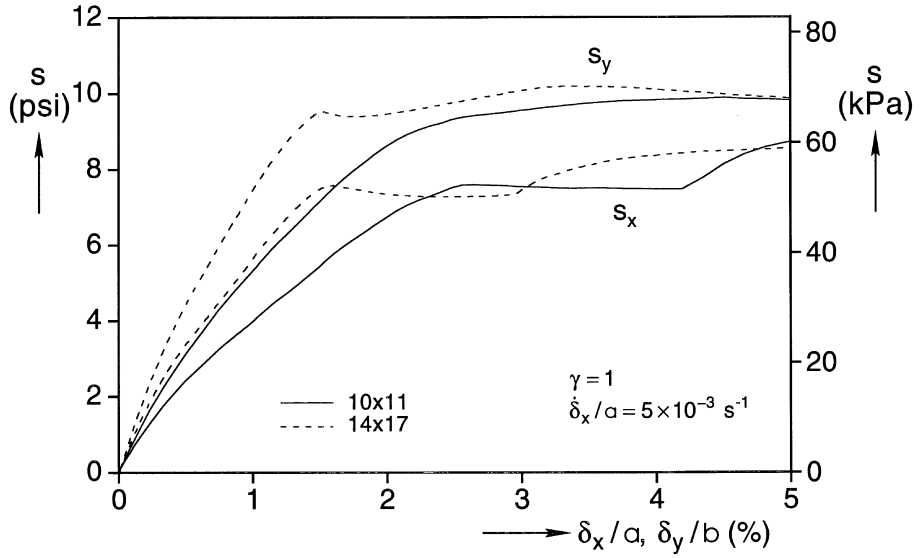

Fig. 8. Comparison of the initial parts of the stress–displacement responses in equibiaxial crushing simulations using 10×11 and 14×17 cell models.

the initial stiffness increases and the extent of the small stress plateau decreases. For average strains higher than 5%, the two sets of responses become very similar.

Friction between the rigid surfaces and the contacting cells also influences these early parts of the responses. To quantify this effect, numerical simulations on the 10×11 cells model were conducted using Coulomb friction coefficients of 0, 0.01, 0.1 and 0.2. The stress–average strain responses up to average strains of 10% are compared in Fig. 9. In the x-direction, increase in μ increases the level and decreases the extent of the initial stress plateau. In the y-direction, increase in μ causes the initiation stress to increase and occur at a smaller value of $\bar{\delta}_y$.

Figure 10a shows a comparison of stress–average strain responses to $\bar{\delta}$ values exceeding 40% for $\mu = 0.01$ and 0.1. Figure 10b shows a set of deformed configurations for $\mu = 0.01$. The biggest deviation between the two sets of responses is for values of $\bar{\delta} < 10\%$. Although some differences between them can also be seen for higher strains, the two pairs of responses stay close to each other. The collapse configurations in Fig. 10b have similar features to those in Fig. 5b but the order of events is different. At lower values of $\bar{\delta}$, there are some obvious differences in the deformation of the cells at the edges of the model (see ① and ② in Figs 5b and 10b). At higher values of $\bar{\delta}$ and for $\mu = 0.01$, deformation first localizes more in the lower left half (see ④ and ⑤) of the model which collapses first while collapse of the other half occurs at higher values of $\bar{\delta}$ (see ⑥). Despite these differences, the overall energy absorption capacity for the two cases is essentially the same.

5.2. *Biaxial test*: $\gamma^{-1} = 0.5$, $\dot{\bar{\delta}}_y = 5 \times 10^{-3}\, s^{-1}$

The second biaxial test that we will discuss in detail is the case of $\gamma^{-1} = 0.5$. The true stress–displacement responses calculated are shown in Fig. 11a along with the corresponding experimental ones. A set of calculated deformed configurations are shown in Fig. 11b. The quality of the predictions is similar to that of the equibiaxial test. The initiation stress in the x-direction is somewhat higher than that of the experiment while in the y-direction, once more, a small initial stress plateau shows up in the analysis but is absent from the experiment. Beyond strains of approximately 10%, the measured and predicted responses are in quite good agreement. The energy absorption of the material per unit undeformed volume at a volume change of 65% is 6.34 psi (43.6 kPa) (Table 4b). This compares with the measured value of 6.16 psi (42.5 kPa).

The deformed configurations are obviously not the same as the experimental ones primarily due to the difference in the specimen size. However, several salient features are common to both sets. For example, the initial deformation of the cells at the edges are very similar. Another common feature is that deformation first localizes in horizontal rows of cells at the top and the bottom of the specimens. At higher values of average strains, a pattern resembling the one shown in Fig. 13[1] is also seen to develop in the center of the model. Interestingly, as was the case for the equibiaxial test, the energy absorption capacity can be predicted to reasonably good accuracy without achieving a one-to-one congruency in the deformed configurations of the experiment and the model.

5.3. *Biaxial test*: $\gamma^{-1} = 3$, $\dot{\bar{\delta}}_y = 5 \times 10^{-3}\, s^{-1}$

The final case to be examined in detail is $\gamma^{-1} = 3$. The calculated stress–average strain responses are compared to the experimental ones in Fig. 12a while deformed configurations from the

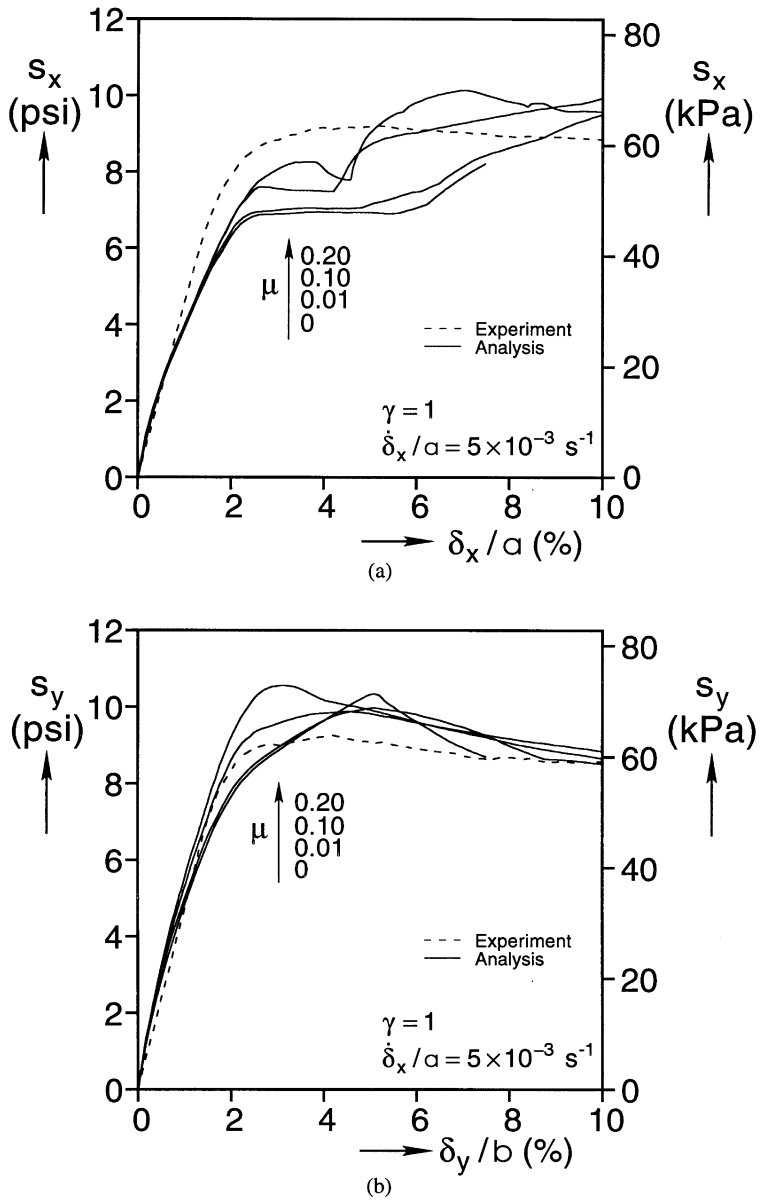

Fig. 9. Effect of Coulomb friction coefficient on the initial parts of the stress–displacement responses in equibiaxial simulation. (a) Responses in the x-direction. (b) Responses in the y-direction.

simulation are displayed in Fig. 12b. In this case, it is the initiation stress in the y-direction that is overpredicted more while in the x-direction the calculated response follows the experimental one quite well. The calculated value for $\mathscr{E}$ is 6.58 psi (45.4 kPa) (Table 4b) which compares well with the measured value of 6.69 psi (46.1 kPa). The collapse patterns yielded by the simulation are again not directly comparable to those of the test due to the difference in specimen size. However,

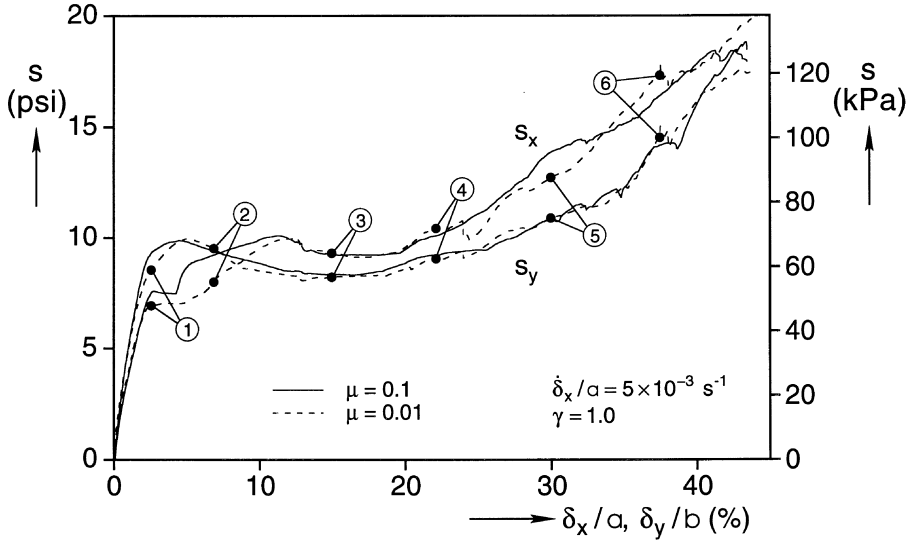

Fig. 10a. Comparison of entire stress–displacement responses from equibiaxial simulations with Coulomb friction coefficients of 0.1 and 0.01.

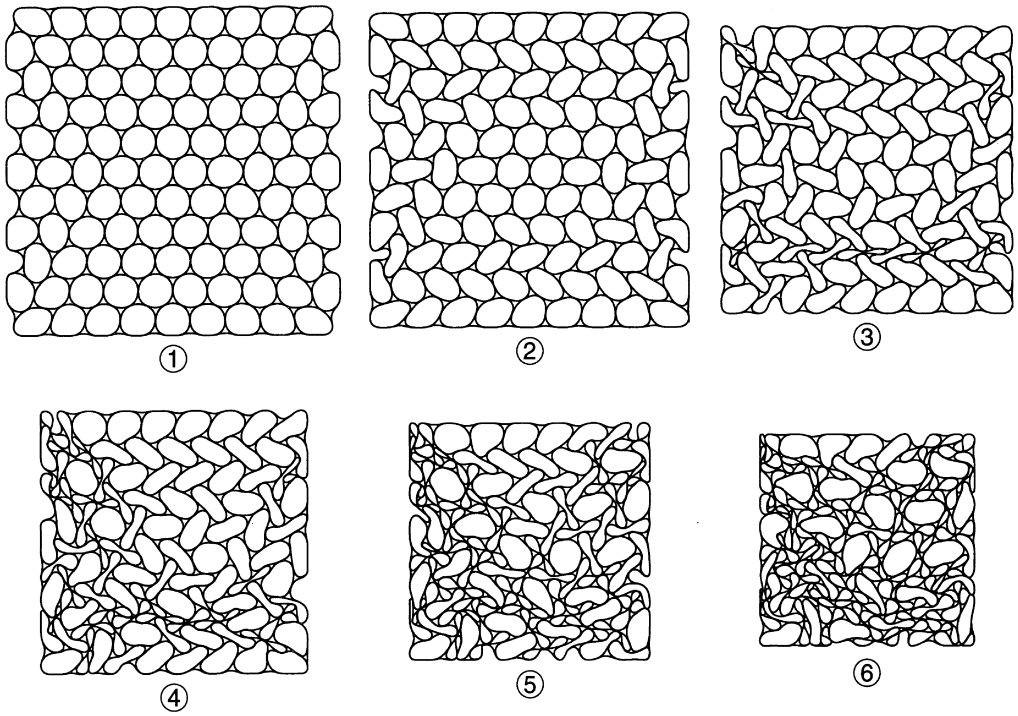

Fig. 10b. Sequence of calculated collapse configurations corresponding to the responses in Fig. 10b with $\mu = 0.01$.

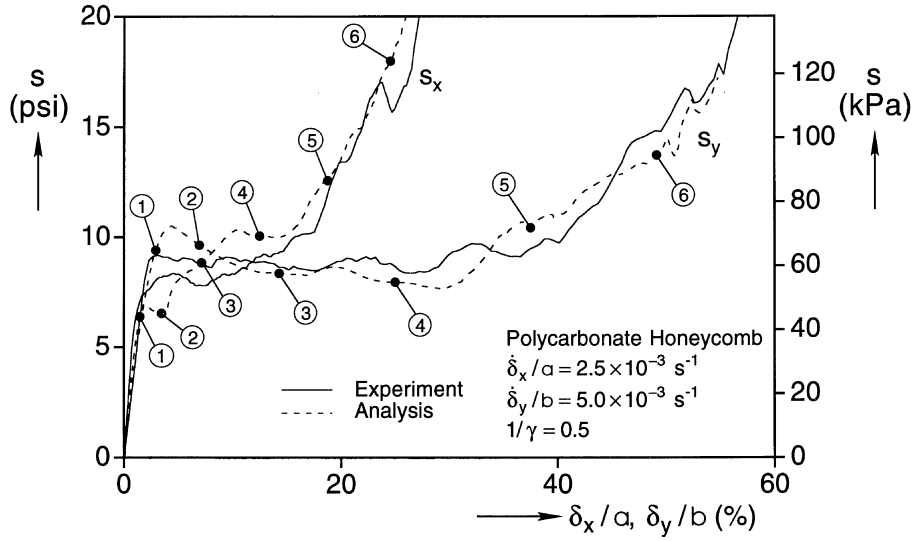

Fig. 11a. Comparison of measured and calculated stress–displacement responses for biaxial crushing with $\gamma^{-1} = 0.5$.

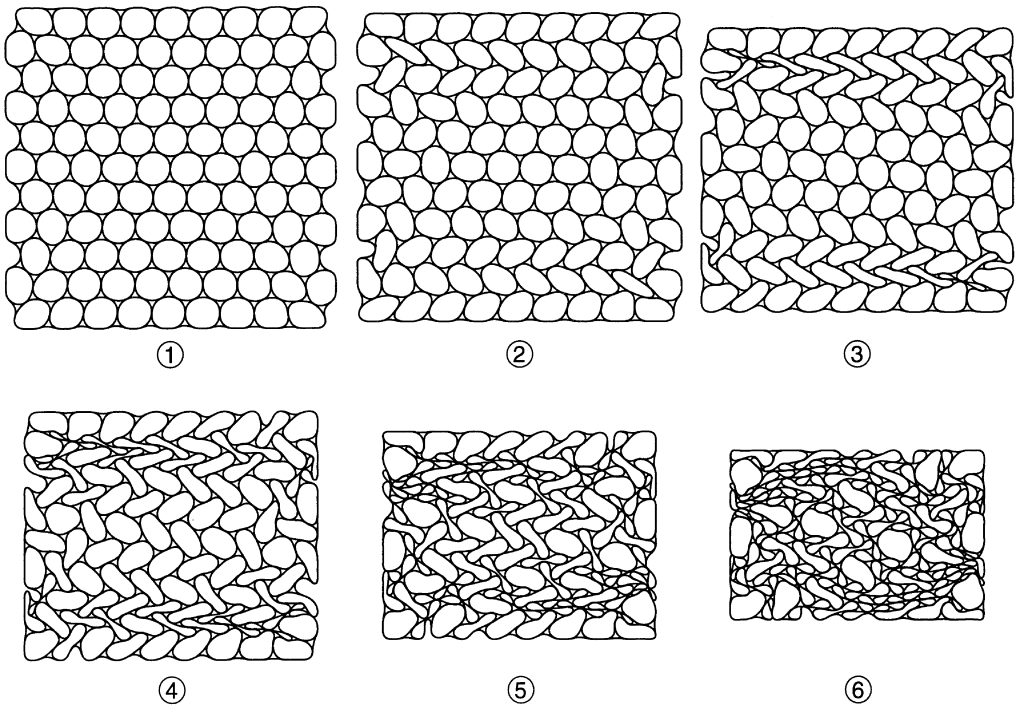

Fig. 11b. Sequence of calculated collapse configurations corresponding to responses in Fig. 11a.

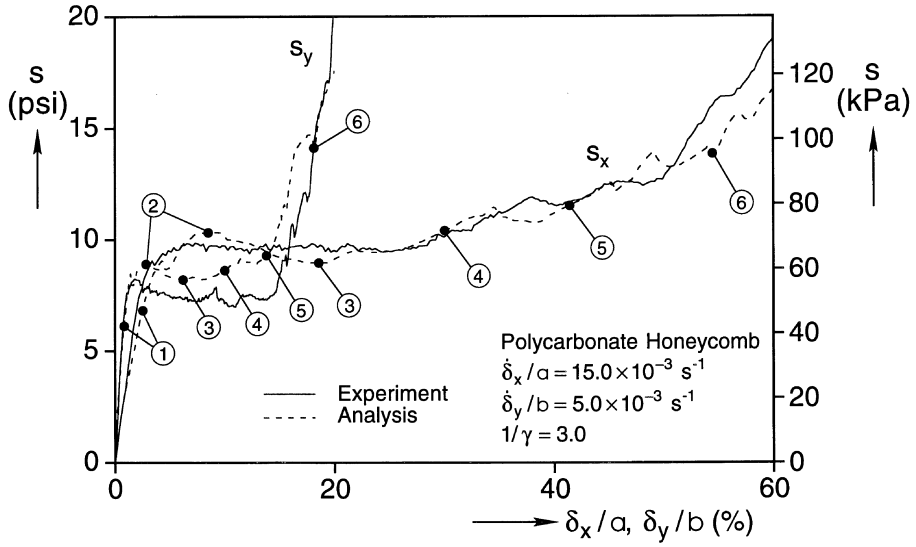

Fig. 12a. Comparison of measured and calculated stress–displacement responses for biaxial crushing with $\gamma^{-1} = 3$.

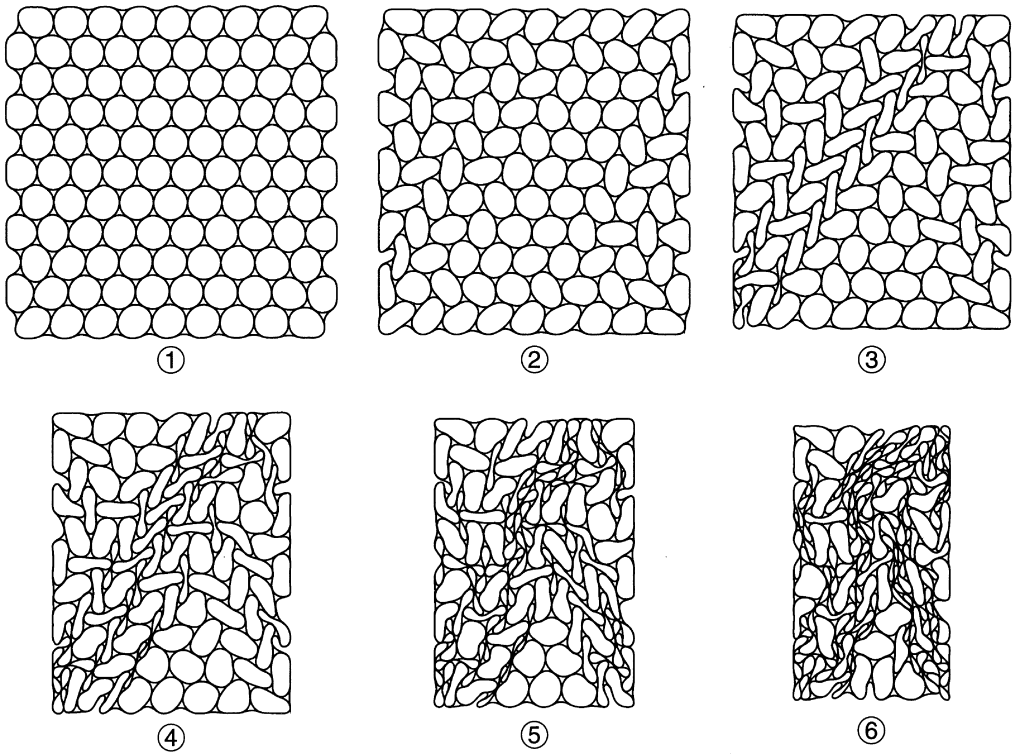

Fig. 12b. Sequence of calculated collapse configurations corresponding to responses in Fig. 12a.

the special pattern reported in Fig. 15[1] does develop in a cluster of cells in the middle of the model in configuration ⑤.

5.4. Broader variation of biaxiality ratios

A total of seven large scale simulations were conducted in which γ and γ^{-1} were varied within the same range of values as those used in the experiments. Results from the additional cases will be shown in summary form for brevity. Figure 13 shows the calculated s_x–$\bar{\delta}_x$ and s_y–$\bar{\delta}_y$ responses from four simulations in which $\gamma = 0$, 0.5, 1 and 3. Figure 14 shows two similar sets of responses for $\gamma^{-1} = 0$, 0.5, 1 and 3. The key problem variables extracted from these responses are listed in Tables 4a and b. The trend seen in the three cases discussed in detail is persistent. The initiation stresses are over predicted to some degree while the energy absorption capacity is calculated to good accuracy. Figure 14 shows a comparison of the calculated and measured initiation stresses vs γ (Fig. 15(a)) and γ^{-1} (Fig. 15(b)). In both cases the values of σ_I are normalized with the initiation stress for the corresponding confined uniaxial test. This normalization reduces the difference between measured and predicted values and shows the analysis to follow the trend of the experiments well. We believe that the calculated values of σ_I would be more quantitatively accurate if the model size was increased to that of the test specimens and if geometric imperfections were included.

A comparison between the calculated and measured values of the energy absorption capacity of the material for the same two sets of experiments is shown in Fig. 16. As alluded to already, this comparison is very favorable.

6. Summary and conclusions

The crushing of polycarbonate honeycomb has been simulated numerically through the finite element method. The model uses appropriately nonlinear kinematics and properly treats the contact that develops between the edges of the model and the rigid walls and between the walls of collapsing cells. The inelastic behavior and rate dependence of the polycarbonate were modeled via elastic–powerlaw viscoplasticity calibrated to experimental material tests. The model is an extension of that used in Papka and Kyriakides (1998a)[1] to simulate uniaxial crushing of the same honeycomb in the y-direction. As in the past, the honeycomb model is assumed to have perfectly circular cells and perfect hexagonal symmetry. The values of the cell diameter, wall thickness and the lengths of the bond lines were assigned the mean values of a set of measurements made on the honeycombs tested. Friction between the rigid surfaces and the edges of the model was represented as Coulomb friction with a coefficient of 0.1. For biaxial crushing, inclusion of friction in the model was found to be necessary for optimum agreement between predictions and measurements.

As in Part I, in order to establish a basis for comparison of the results of biaxial analyses, the paper includes a brief review of results from a one-to-one simulation of a uniaxial crushing test in the y-direction and an exposé of a similar simulation of the x-crushing test in Part I. Both uniaxial simulations are in very good agreement with the corresponding experiments.

The size of the specimen used in the biaxial crushing experiments (18×21 cells) is significantly larger than those used in the uniaxial crushing work. In addition, because of the more complex

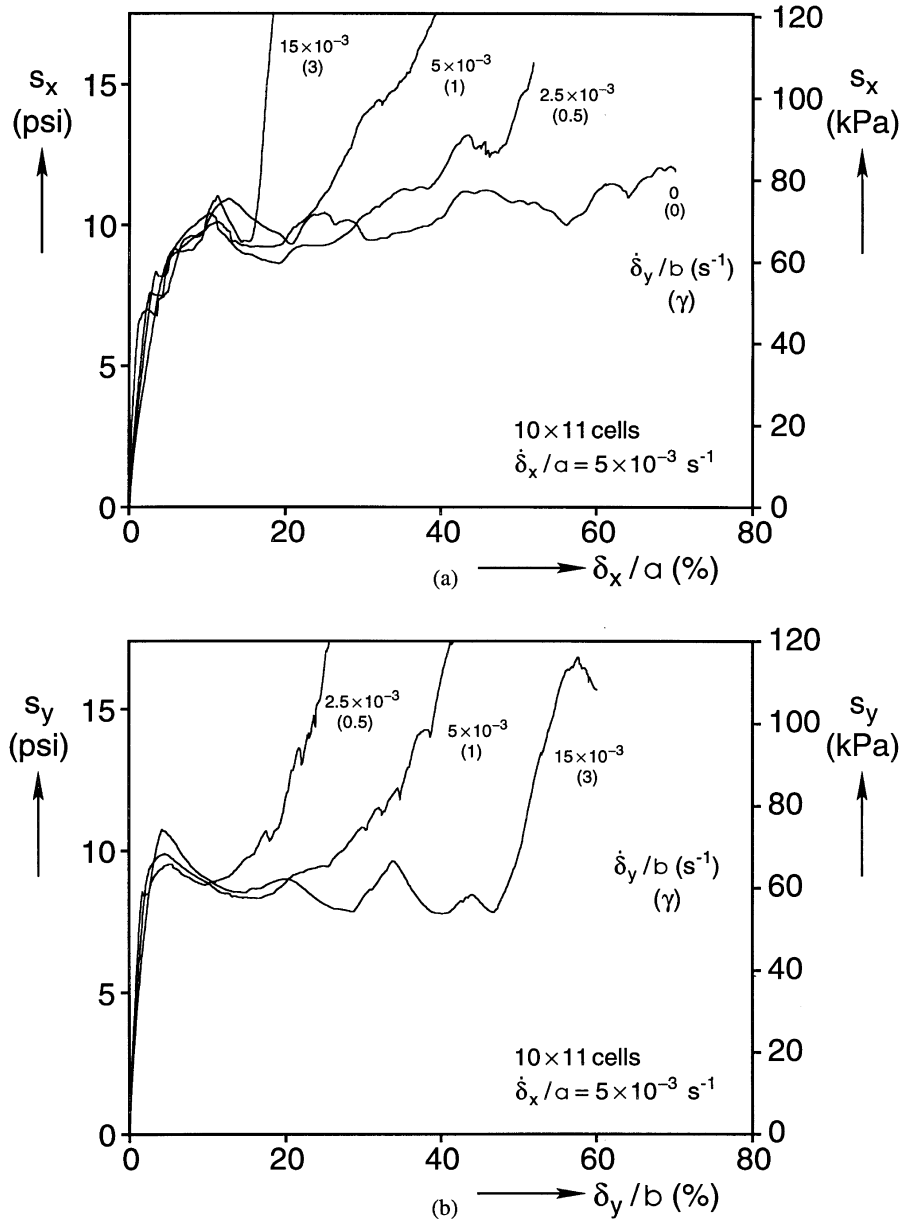

Fig. 13. Calculated stress–displacement responses from crushing simulations involving various values of γ and $\dot{\delta}_x = 5\times10^{-3}\ s^{-1}$. (a) x-direction and (b) y-direction.

deformation patterns that develop and of the more complex contact that takes place, the size of the problems that must be solved during each iteration is significantly larger. As a result, and because of limitations in the computational resources available for these simulations, the size of the model analyzed had to be limited to 10×11 cells.

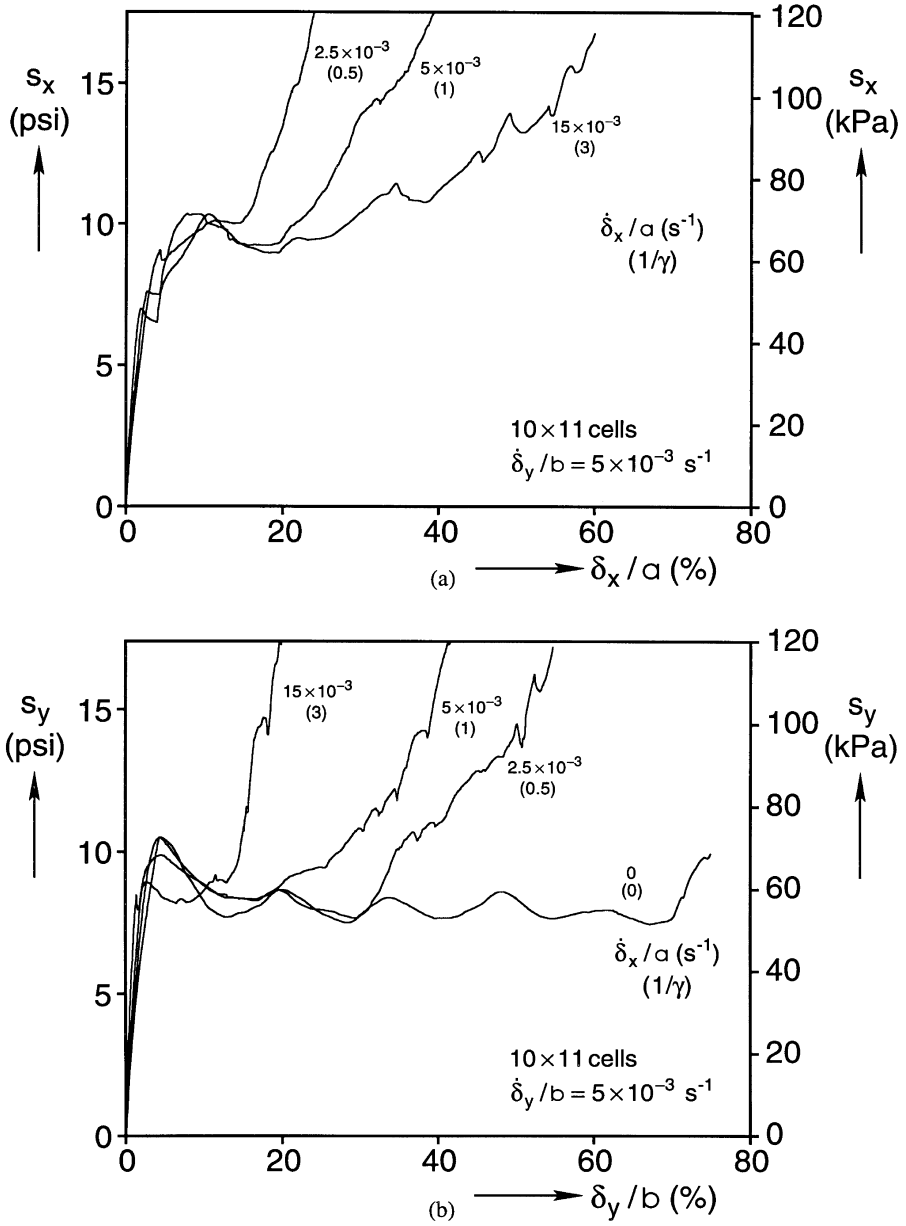

Fig. 14. True stress–displacement responses from the series of tests conducted at various values of γ^{-1} and $\dot{\bar{\delta}}_y = 5 \times 10^{-3}$ s^{-1}. (a) x-direction and (b) y-direction.

As indicated in Part I, edge effects, specimen size and friction have an effect on the crushing response. The effect of these parameters was studied parametrically in the case of equibiaxial crushing. The size of the specimen was shown to affect the initial elastic parts of the responses and the onset of instability ('knees' in s–$\bar{\delta}$). Smaller specimens were shown to have softer initial

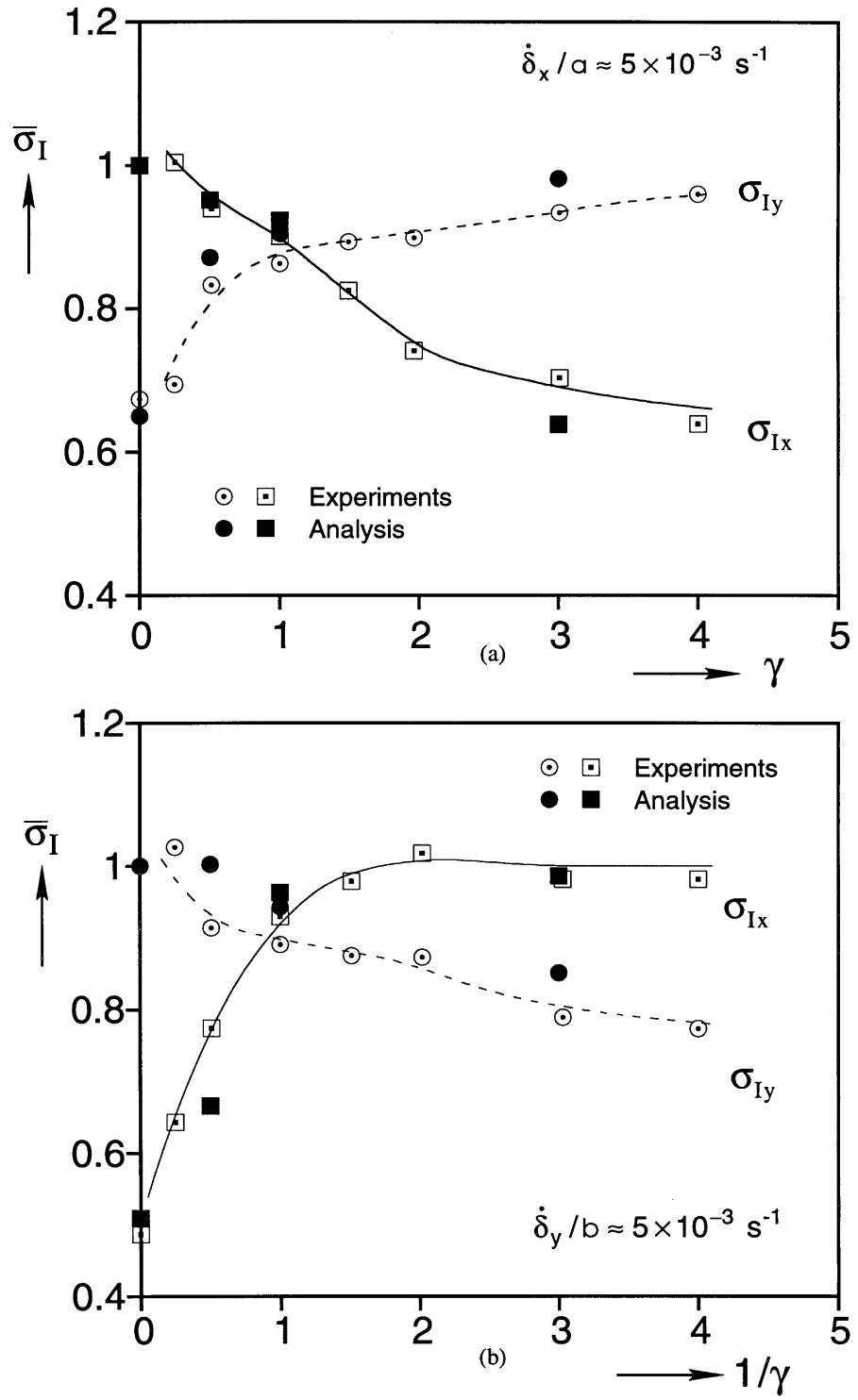

Fig. 15. (a) Measured and calculated initiation stresses in two directions as a function of γ. (b) Measured and calculated initiation stresses in two directions as a function γ^{-1}.

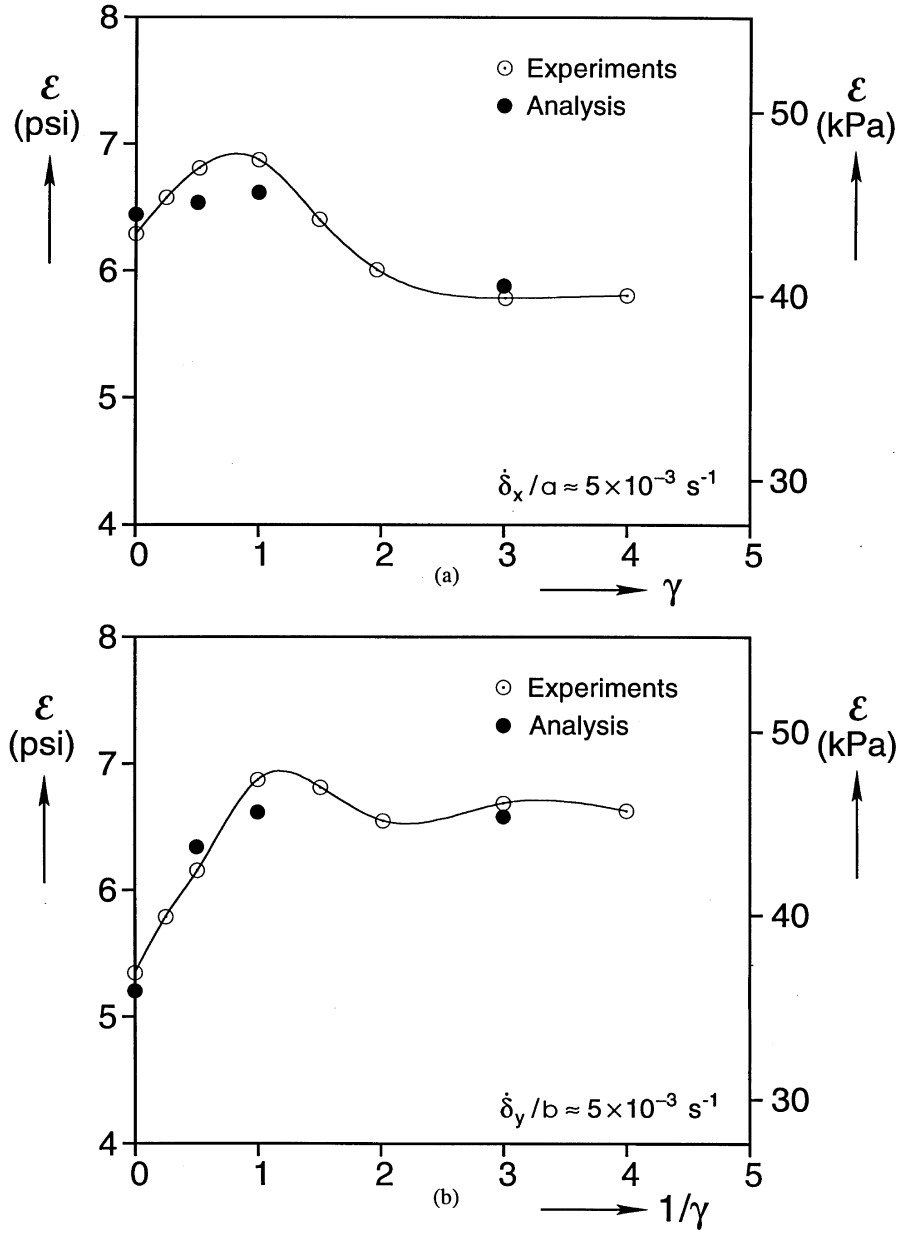

Fig. 16. (a) Comparison of measured and calculated crushing energy as a function of γ. (b) Comparison of measured and calculated crushing energy as a function of γ^{-1}.

responses and somewhat lower initiation stresses. However, for specimens with 10×11 and 14×17 cells, the stress–displacement responses tended to be very similar for average strains higher than approximately 5%. Similarly, the predicted responses differed to some degree from the experimental ones on 18×21 cell specimens in the early stages of crushing but compared quite favorably for

average strains higher than approximately 8%. This occurs, despite the fact that the collapse patterns seen in the simulations were not the same as those in the experiment. This difference is mainly attributed to the smaller size of the specimen in the model and, to a lesser degree, to the absence of geometric imperfections in the model. However, the similarity between the deformed patterns and the prevalent crushing mechanisms seen in the simulations and experiments lead us to expect that, if the model size is increased to match that of the tests, the crushing patterns will become much closer to those reported in Part I.

Friction between the edges of the specimen and the rigid surfaces surrounding it was found to also influence the early part of the responses and, in particular, the onset of instability and the initiation stresses. As a consequence, this also affects the deformation patterns that develop at higher average strains. We found that the inclusion of friction made the predictions both quantitatively and qualitatively closer to the experimental results for average strains less than approximately 10%. Once more, at higher values of average strains the effect of friction on the calculated responses was not very significant.

Results from seven full scale crushing simulations were presented for various values of γ and γ^{-1}. The quality of the predictions vis-à-vis the experiments is similar in all cases to those of the equibixial case. The early part of the calculated responses and the initiation stresses differ to some degree from those of the experiments. At higher values of strains, the predicted responses agree well with the experimental ones. The energy absorption capacities up to volume reductions of 65% are in very good agreement with the experimental values for all cases.

In conclusion, full scale numerical simulations of biaxial crushing can successfully predict the major material parameters of interest. Experiments as well as numerical simulations on finite size specimens introduce some errors in the initial elastic properties and to some degree to the level of the initiation stresses. Both of these variables can be predicted more accurately using simpler techniques involving small characteristic cells (e.g. see Appendix of Papka and Kyriakides (1998a)[1] for elastic properties, Triantafyllidis and Schraard (1998)[1] for initiation stresses under biaxial loading conditions). Simulations of the type presented here are a viable tool for establishing the response of the material at higher stages of crushing and its energy absorption capacity.

Acknowledgments

The financial support of the Air Force Office of Scientific Research under grant number F49620-98-1-0145 is acknowledged with thanks. We are grateful to Hibbitt, Karlsson and Sorensen, Inc. for making ABAQUS available under academic license.

References

Gibson, L.J., Ashby, M.F., Zhang, J., Triantafillou, T.C., 1989. Failure surfaces for cellular materials under multiaxial loads—I. Modeling. Int. J. Mechanical Sciences 31, 635–663.

Peirce, S.D., Shih, C.F., Needleman, A., 1984. A tangent modulus method for rate dependent solids. Computers and Structures 18, 875–887.

Triantafillou, T.C., Gibson, L.J., 1990. Multiaxial failure criteria for brittle foams. Int. J. Mechanical Sciences 32, 479–496.

Triantafillou, T.C., Shercliff, T.L., Gibson, L.J., Ashby, M.F., 1989. Failure surfaces for cellular materials under multiaxial loads—II. Comparison of models with experiments. Int. J. Mechanical Sciences 31, 665–678.